CHEMISTRY OF MATERIALS

pubs.acs.org/cm

Article

Thermal Decomposition of Magnesium Borohydride: New Insights from Synchrotron X-ray Scattering

Nicholas A. Strange, Noemi Leick, Robert T. Bell, Margaret A. Fitzgerald, Svitlana Pylypenko, Andreas Schneemann, Vitalie Stavila, and Thomas Gennett*

Cite This: *Chem. Mater.* 2022, 34, 10940−10951

Read Online

ACCESS | Metrics & More | Article Recommendations | Supporting Information

ABSTRACT: Magnesium borohydride [$Mg(BH_4)_2$] has been extensively investigated as a promising material with applications in energy storage, having properties favorable for both hydrogen and electrochemical storage processes. Recent efforts regarding hydrogen storage to determine conditions optimal for dehydrogenation and hydrogenation have focused on identifying environmental factors that promote various polyborane intermediate pathways. In the present study, we demonstrate the impact of the synthesis route, residual impurities, sample processing, and starting crystalline phase on the structural transformations and decomposition pathways of $Mg(BH_4)_2$. Using synchrotron powder X-ray diffraction (PXRD) and small-angle X-ray scattering (SAXS), we provide evidence of the residual dimethyl sulfide solvent coordinated inside the pores of γ-$Mg(BH_4)_2$ even after post-synthetic de-solvation. In situ temperature-resolved PXRD and temperature programed desorption (TPD) indicate that these impurity molecules are removed by heating to 100 °C in vacuo. Furthermore, when γ-$Mg(BH_4)_2$ is heated slowly under vacuum, we observe a γ- to α-phase transformation in place of the ε-$Mg(BH_4)_2$ "intermediate" structure, which provides a direct connection between the α- and γ-$Mg(BH_4)_2$ decomposition pathways. At higher temperatures (~150 °C), $Mg(BH_4)_2$ transitions to the well-known β-phase structure. Although XRD results suggest that the crystalline structures of β-$Mg(BH_4)_2$ are identical regardless of the starting material, SAXS and transmission electron microscopy indicate that when the γ-phase is used as the starting structure, the resulting β-$Mg(BH_4)_2$ material exhibits intergranular (i.e., skeletal) porosity, not observed when annealed from the α-phase. These variations of the microstructure may contribute to differences in dehydrogenation mechanisms observed in TPD data among the three currently existing "as-synthesized" $Mg(BH_4)_2$ structural phases.

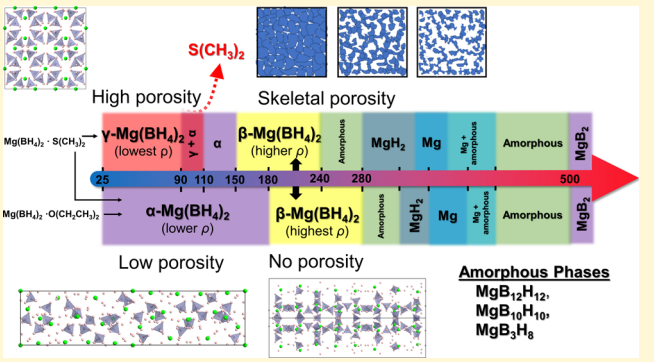

INTRODUCTION

Complex hydrides display a number of material properties desirable for efficient hydrogen- or electrochemical-based energy storage. Magnesium borohydride, $Mg(BH_4)_2$, is one such compound that is considered a leading contender for material-based hydrogen storage due to its 14.9 wt% gravimetric H_2 capacity; however, its technological deployment is hindered by poor dehydrogenation reversibility,[1] slow reaction kinetics,[2] and high temperatures required for decomposition and hydrogen release.[3] On the other hand, the moderately high decomposition temperatures and slow reaction kinetics of $Mg(BH_4)_2$ are considered favorable properties for its implementation as a Mg-ion conducting electrolyte.[4]

One substantial barrier impeding the development of $Mg(BH_4)_2$ as a hydrogen storage material or electrolyte is the accurate determination of temperature-dependent structural phase transformations and decomposition reaction pathways. Multiple reports[5−9] indicate that upon heating to ~335 °C, $MgB_{12}H_{12}$ is formed as the primary decomposition product. Alternatively, if $Mg(BH_4)_2$ is heated to 200 °C for 5 weeks, some quantity is converted to $Mg(B_3H_8)_2$, though no formation of MgH_2 is observed as is suggested by the authors' proposed reaction equation.[10] The proposed mechanisms of these dehydrogenation reactions have not been conclusively confirmed, as several unidentified boron environments have been observed by ^{11}B NMR in decomposed $Mg(BH_4)_2$ samples with inconsistencies in the identities, quantities, and temperatures of formation existing among published accounts.[6] Nevertheless, $Mg(BH_4)_2$ polymorphs exhibit unique structural features akin to those of framework materials which set them

Received: September 23, 2022
Revised: November 18, 2022
Published: December 7, 2022

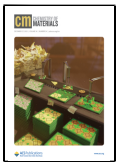

apart from similar complex hydrides and, given the uncertainties in the literature, present an opportunity for a compelling fundamental study on structure−property relationships.

$Mg(BH_4)_2$ exhibits rich polymorphism with six experimentally observed structural phases[11−14] in addition to a number of theoretical structures.[15−19] Relative to other metal borohydrides, $Mg(BH_4)_2$ exhibits structural properties intermediate to the smaller-cation borohydrides (Li, Be) and larger-cation borohydrides (Na, K, Ca).[11] For example, in $Mg(BH_4)_2$, magnesium atoms are tetrahedrally coordinated to BH_4 groups in comparison to trigonal coordination in $Be(BH_4)_2$ and octahedral coordination in $Ca(BH_4)_2$.[20] The cause of magnesium borohydride's "hybrid" behavior has been suggested to result from the magnesium cation's intermediately sized ionic radius.[20] The first crystal structure obtained for a sample of α-$Mg(BH_4)_2$ was solved independently by Her et al.[11] and Černý et al.[20] using powder X-ray diffraction (PXRD) methods. The low-temperature hexagonal α-phase was first reported with $P6_1$ symmetry[11] and later amended to $P6_122$ after refinement of single-crystal X-ray diffraction data.[21] Both reports noted that as the α-phase was heated to ∼180 °C, a structural transformation to the high-temperature orthorhombic β-phase was observed.[11,21] Ozolins et al.[17] suggested that the ground-state α-$Mg(BH_4)_2$ structure is ∼5 kJ/mol lower in energy than the β-phase based on density functional theory calculations and is likely the low-temperature stable structure between the two phases. More recently,[12] a cubic mesoporous γ-phase was synthesized which contains 33% theoretical void space. The γ-phase was initially celebrated for its hybrid physical/chemical hydrogen storage properties in addition to its high surface-to-volume ratio, compared to that of the other known phases, which was expected to enhance hydrogen diffusion (and release of H_2) during decomposition but seemingly faces the same mass transport challenges of the other structural phases.[5,22,23] It has been hypothesized that additional $Mg(BH_4)_2$ phases that display structures analogous to experimental or theoretical zeolitic framework structures could potentially exist.[5]

In terms of local structures, the known crystalline phases of $Mg(BH_4)_2$ all appear to contain Mg atoms tetrahedrally coordinated to BH_4 tetrahedron edges with eight-coordinate bidentate hydrogen interactions (μ_2-H_2). In general, the BH_4 groups can be characterized as distorted tetrahedra where pairs of hydrogen atoms oriented toward Mg atoms exhibit a widened angle. The $Mg(BH_4)_4$ tetrahedra are also considerably deformed with the extent of distortion dependent on the phase. In α-$Mg(BH_4)_2$, the three symmetry-inequivalent Mg sites are relatively similar in their local geometries. The same cannot be said for Mg atoms in the orthorhombic β-phase. Additionally, the α-phase exhibits ∼6.4% void space which forms a corkscrew-shaped pore structure about the 6_1 axis oriented along the c-direction.[12] Using a probe radius of 1.2 Å, the void space of α-$Mg(BH_4)_2$ was reported to be eradicated as the material transforms to the β-phase. The γ-phase stands alone as the only polymorph observed to exhibit large permanent porosity. The γ-phase's cubic structure is highly symmetric with Mg and B atoms residing on special sites, while two distinguishable H atoms are located at general sites.

Two methods for synthesizing $Mg(BH_4)_2$ have been previously reported. The first mechanism involves an exchange reaction between a metal borohydride and metal halide in diethyl ether or similar ether-based solvents.[24]

$$2NaBH_4 + MgCl_2 \xrightarrow{\Delta} Mg(BH_4)_2 + 2NaCl \quad (1)$$

This route yields only α- or β-$Mg(BH_4)_2$ depending on whether the de-solvation temperature is maintained above or below ∼180 °C, respectively.[11] The second and more recently discovered method[25] involves a metathesis reaction between $Mg(C_4H_9)_2$ in n-heptane and the borane adduct of dimethyl sulfide (DMS), $BH_3{\cdot}S(CH_3)_2$, in toluene with a proposed reaction equation:

$$3Mg(C_4H_9)_2 + 8BH_3{\cdot}S(CH_3)_2 \rightarrow 3Mg(BH_4)_2{\cdot}2S(CH_3)_2 + 2B(C_4H_9)_3{\cdot}S(CH_3)_2 \quad (2)$$

More recently, Richter et al. proposed an alternative pathway for synthesizing γ-$Mg(BH_4)_2$ which involves reacting MgH_2 with borane DMS, bypassing the use of the organomagnesium reactant, but leads to the same intermediate DMS complex in eq 2.[26] One of the major challenges with these synthesis pathways is the use of coordinating complexes and/or electron-donor solvents. From the synthesis starting with the organomagnesium compound, dissociation of DMS adduct species can only be achieved with vacuum or gentle heating. If heated ≤85 °C, the γ-phase is the preferred product, but if heat-treated near 150 °C, the α-phase forms.[27] The literature contains a number of conflicting results on the decomposition phase diagram of $Mg(BH_4)_2$ which is presumably, in part, due to the method of synthesis, post-treatment, and sample handling.[5,8,9,11,22,28,29] The existing discrepancies underscore the need for controlled sample handling and in situ characterization to understand the impacts of processing. Stadie et al.[30] reported a supercritical nitrogen processing method for removing impurities, including residual synthesis products, from γ-$Mg(BH_4)_2$ which subsequently reduced the formation/release of diborane (B_2H_6) at low temperatures. However, no literature is available on the identification and quantification of residual impurities and how they influence material decomposition.

In the current study, a series of synchrotron X-ray scattering measurements were used to provide a fundamental physicochemical understanding of the γ-$Mg(BH_4)_2$ structure and decomposition mechanism. New insights obtained by this investigation build upon the existing body of the literature and address some of the prevailing uncertainties about the structures and phase transformations. Special attention was directed toward the importance of the synthesis route, any resulting defects, and residual impurities in relation to how they influence material decomposition and hence impact the temperature of hydrogen release, hydrogen capacity, and purity. In situ temperature-resolved X-ray scattering measurements, specifically synchrotron radiation PXRD and small-angle X-ray scattering with simultaneous wide-angle scattering (SAXS/WAXS), were conducted with varying experimental conditions (e.g., dynamic vacuum, ambient pressure, and hydrogen backpressure). To-date, SAXS has been largely underutilized for examining the mesoporous structure of magnesium borohydride polymorphs. Prior SAXS examinations of hydrogen storage materials have been limited to infiltration of hydrides into activated carbons[2,31] and physisorption in porous frameworks.[32] The results obtained from structural measurements are related to the decomposition properties with temperature programed desorption (TPD) where it is shown that the starting phase and synthesis method lead to drastically different temperatures and quantities of

https://doi.org/10.1021/acs.chemmater.2c02925
Chem. Mater. 2022, 34, 10940−10951

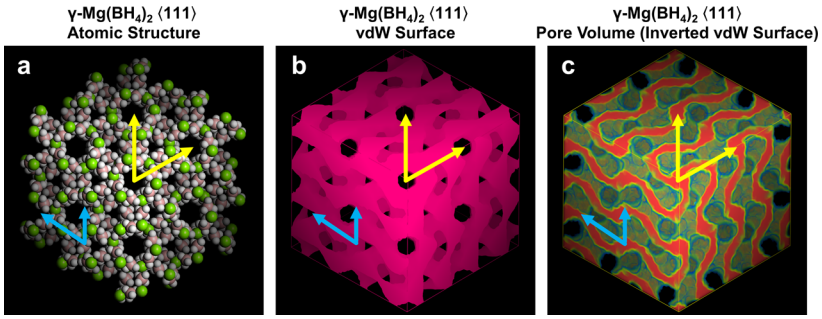

Figure 1. (a) γ-$Mg(BH_4)_2$ (2 × 2 × 2 supercell) viewed down the ⟨111⟩ direction alongside the (b) calculated vdW surface (represented by a magenta isosurface) and (c) pore volume (represented by a red isosurface). In (a), Mg atoms are green, B atoms are pink, and H atoms are white. Spatial correlations of pores are highlighted along the cubic facets (blue arrows) and diagonals (yellow arrows).

hydrogen release. Structure−property relationships provided by this combination of highly sensitive techniques not only remedy some of the conflicting results and structural ambiguities in the literature but also provide new information on best practices for material processing and handling which can lead to more efficient design and development of complex hydrides for energy storage applications.

EXPERIMENTAL SECTION

Synthesis. Both α- and γ-phases of magnesium borohydride were synthesized using a slightly modified version[33] of the route described in eq 2, a synthesis method published previously by Zanella et al.[25] In order to prepare phase-pure γ-$Mg(BH_4)_2$, the $Mg(BH_4)_2{\cdot}S(CH_3)_2$ adduct was dried under vacuum and subsequently heated to 85 °C in vacuo. A more detailed procedure is presented elsewhere.[27] When the adduct material is dried under argon for 1 day, followed by heating to 160 °C under vacuum overnight, α-$Mg(BH_4)_2$ is the primary product. A second batch of α-magnesium borohydride was also purchased from Sigma-Aldrich.

Temperature Programed Desorption. TPD measurements were performed in a custom-built instrument described in detail elsewhere.[34] In a helium glovebox, 1−2 mg of magnesium borohydride was packaged in platinum foil to ensure homogeneous heating of the entire sample and sealed in a quartz tube. The tube was connected to the TPD instrument and subsequently evacuated to $\leq 10^{-8}$ Torr. The quantity of the material was adjusted to stay within the calibrated mass spectrometer's linear response region. The sample was heated between room temperature and 500 °C with a 15 °C/min heating rate under dynamic vacuum. Gaseous species evolved during decomposition were detected using an SRS RGA 100 with a 70 eV ionization energy with a sampling rate of 2−4 s, depending on the m/z range scanned (e.g., 1−50 vs 1−100). The resulting signals were normalized to sample mass.

Surface Area and Porosimetry. Nitrogen physisorption isotherms from the neat and heated $Mg(BH_4)_2$ samples were measured in a Micromeritics ASAP 2020 apparatus at 77 K. Data was collected with 45 s equilibration time in the p/p_0 range of 0−0.001 which was decreased to 10 s for $p/p_0 > 0.001$. The specific surface area and pore size distributions (PSDs) of the samples were extracted from these isotherms, where the Rouquerol criterion was satisfied. The relative pressure regimes for the Brunauer−Emmett−Teller (BET) analysis were chosen in the range according to the criteria for evaluating BET surface areas of microporous materials:[35] p/p_0 from 0 to 0.012 for neat $Mg(BH_4)_2$, p/p_0 from 0 to 0.03 for $Mg(BH_4)_2$ heated to 100 °C, and p/p_0 from 0 to 0.1 for $Mg(BH_4)_2$ heated to 200 °C. PSDs were analyzed using a Micromeritics NLDFT model for N_2 adsorption on carbon. The model selected was a PSD for mesoporous and microporous carbon with pores from 3.5 to 1000 Å with an infinite slit pore assumption, based on previous analysis.[36]

Transmission Electron Microscopy. Transmission electron microscopy (TEM) images were obtained on the FEI Talos F200X in the scanning mode at 200 keV with ∼15 s exposures. Specimens were prepared in an argon atmosphere without solution or sonication. Samples were deposited on copper reference grids with a carbon mesh (Ted Pella, Inc.) and packaged in air-sealed aluminum packets for transport to the microscope. Once removed from the package, samples were immediately placed on the holder and inserted into the transmission electron microscope, resulting in ∼2 min of air exposure. Samples were imaged using an identical location microscopy approach in which individual particles were identified, tracked, and imaged before and after heating to 250 °C. After initial imaging, samples were removed from the holder and immediately brought to the glove box, which results in an additional 4 min of air exposure. Once returned to the glove box, TEM grids were heated for 20 min under an argon atmosphere using a temperature-monitored hot plate and packaged for subsequent imaging to observe the samples after heating. The samples were exposed to air for ∼2 min when transferred into the microscope. Samples were re-imaged using the same conditions as those used during imaging of fresh samples using notes based on the reference grid.

Elemental Analysis. Elemental quantifications were conducted in the microanalytical laboratories at Galbraith Laboratories (Knoxville, TN) using an elemental analyzer for combustion analysis.

X-ray Scattering Measurements. X-ray scattering measurements were conducted at the Stanford Synchrotron Radiation Lightsource (SSRL). Simultaneous SAXS/WAXS measurements were performed at SSRL beamline 1-5 in transmission geometry utilizing a 1 m sample-to-detector configuration and a photon wavelength of 0.7999 Å. Two-dimensional images were acquired with Rayonix 165 CCD (SAXS) and Dectris PILATUS 100K (WAXS) detectors. SAXS/WAXS data was reduced and analyzed using the Nika[37] and Irena[38] macros in Igor Pro. PXRD data was measured in Debye−Scherrer geometry at SSRL beamlines 2-1 (λ = 0.729 Å) and 7-2 (λ = 0.8854 Å) using a PILATUS 100K detector with portrait orientation. 2D images were integrated and stitched into a 1D diffraction pattern using an in-house-developed Python script. Samples used in the X-ray scattering measurements were prepared in 1 mm quartz capillaries with 10 μm wall thickness purchased from Charles Supper Company, Inc. The capillaries were sealed in a sample cell described elsewhere[39] with Swagelok compression fittings. The cell was connected to a gas-handling manifold which utilized three different sample environments: dynamic vacuum (base pressure of 13.33 mbar), atmospheric pressure argon, and 5 bar hydrogen backpressures. In situ sample cooling was achieved with an Oxford Cryostream.

Structural refinements of the in situ PXRD patterns were performed using the Rietveld method in GSAS-II.[40] Void space calculations on the refined crystal structures of $Mg(BH_4)_2$ were carried out using the VOID routine in the PLATON[41] multipurpose crystallographic tool. The resulting isosurfaces were generated and visualized in Jmol.[42]

https://doi.org/10.1021/acs.chemmater.2c02925
Chem. Mater. 2022, 34, 10940−10951

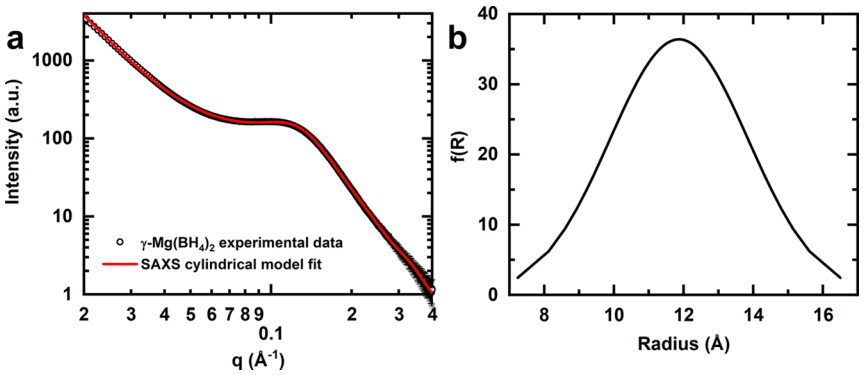

Figure 2. (a) Experimental SAXS data (black circles) from γ-$Mg(BH_4)_2$ and the corresponding size distribution fit (red line) to the experimental data using a cylindrical form factor (aspect ratio = 3.5). (b) Size distribution of cylindrical pore lengths, $f(R)$, derived from the SAXS model.

RESULTS AND DISCUSSION

Structure of γ-$Mg(BH_4)_2$. The reported crystal structure of γ-$Mg(BH_4)_2$ is body-centered cubic ($Ia\bar{3}d$, space group230) with lattice parameter a = 15.7575 Å.[12] The material's crystal structure exhibits an inter-connecting 3D porous network (see Figure 1a–c), similar to that of some mesoporous silicas (e.g., KIT-6, FDU-5). The pore structure is a double gyroid composed of hexagonal close-packed (HCP) cylindrical pores oriented along the four space diagonals of the cubic unit cell which are highlighted by the van der Waals (vdW) surface displayed in Figure 1b. Each of the cylindrical pores is interpenetrated by undulating channels which are oriented in directions parallel to the unit cell vectors depicted by the volume shown in red in Figure 1c. Using the radius of the hydrogen atom as a gauge of "useable porosity," these undulating channels do not appear to exhibit extended porosity and are limited to volumes having maximum length components of roughly 25% of the lattice parameter, separated by narrowed regions at the crests and troughs observed in Figure 1c. Although no two cylindrical pores directly bisect one another, adjacent cylindrical pores oriented along opposing directions are inter-connected by voids situated at points tangential to the cylinder surfaces.

Locally, the cylindrical pores are constructed from alternating stacks of hexagonally and trigonally arranged BH_4^- units with Mg cations staggered above and below the geometric plane between each pair of anions (see Figure S1). The BH_4^- units are rotated by 30° about the long axis of the cylindrical pores in between adjacent layers. In turn, the screw axis creates six helical chains of BH_4—three of which are continuous and three are discontinuous in alternating layers. The discontinuities in the helical chains give rise to the voids which connect adjacent cylindrical pores.

SAXS was used to experimentally investigate the pore structure of γ-$Mg(BH_4)_2$ as-synthesized. The SAXS pattern from γ-$Mg(BH_4)_2$ is provided in Figure 2a. The observation of a Guinier feature near $q \sim 0.1$ Å was surprising, considering that long-range void space (e.g., extending beyond multiple unit cells) along the length of the cylindrical pores should cause such a feature to appear with a much larger d-spacing (lower q). Given the known gyroidal pore structure depicted in Figure 1c, we initially tried to fit the SAXS data in Figure 2 with a "two-level" structural model described by the unified exponential/power law approach since the geometries of individual pores can be represented by a cylinder with a high aspect ratio (i.e., a rod[a]). However, the experimental SAXS data displayed in Figure 2a could not be appropriately fit with the unified exponential/power law approach, which indicated that the observed SAXS intensity was more complex than the simple two-level structure of a rod. We speculated that the fit should also account for polydispersity of cylindrical pore lengths, which is a feature that the unified exponential/power law approach is ill-equipped to model. Adding to this complexity, the SAXS intensities produced by the cylindrical pores are influenced by spatial correlations due to the ordered pore structure (see Figure 1c) and require the inclusion of a structure factor contribution to the SAXS model. The first and second nearest neighbor distances between pores in the HCP network are ~12.5 (q = 0.5 $Å^{-1}$) and ~22.5 Å (q = 0.28 $Å^{-1}$), respectively. The most physically reasonable fit to the SAXS data, shown in Figure 2a, involved modeling a cylindrical form factor with a Gaussian distribution of pore lengths. The aspect ratio of the cylinder was restricted to values that fixed the pore radius at 3.5 Å since this quantity should be largely invariable. The structure factor contributions to the intensity were modeled using a method similar to that of a hard sphere model[43] and provided an average correlation length of 43.9 ± 1.4 Å (packing factor of 2.9) which is 3.5 times the value of the nearest neighbor distance of HCP cylindrical pores. The resulting volume distribution of radii is shown in Figure 2b, which suggests that the average cylinder length is approximately 23.7 ± 4.0 Å. The mean value is ~85% of the length of the cubic space diagonal of the unit cell (27.29 Å), which suggests that the pores do not exhibit extended porosity but rather are occluded.

In order to investigate why the pore size of γ-$Mg(BH_4)_2$ calculated from the SAXS data was comparable to the length across a single unit cell, we used PXRD to identify any notable crystalline (e.g., pore collapse) or atomic-scale defects (e.g., inclusions) to the material. PXRD measurements were acquired on a sample of γ-$Mg(BH_4)_2$ at room temperature and again after cooling to approximately 120 K as shown in Figure 3. The PXRD pattern of γ-$Mg(BH_4)_2$ at room temperature is consistent with the structure determined by Filinchuk et al.[12] However, upon cooling to ~120 K, three new diffraction peaks (corresponding to the 400, 332, and 521 Miller indices) were identified together with several changes in peak intensities of overlapped reflections at higher diffraction angles. At room temperature, the 400, 332, and 521 reflections are not observable since they are associated with "unoccupied" sites within the porous γ-$Mg(BH_4)_2$ structure. Guest molecules appear to be diffuse at room temperature but order upon cooling. Recalling that $Mg(BH_4)_2 \cdot 0.5\ S(CH_3)_2$ is formed as an

https://doi.org/10.1021/acs.chemmater.2c02925
Chem. Mater. 2022, 34, 10940−10951

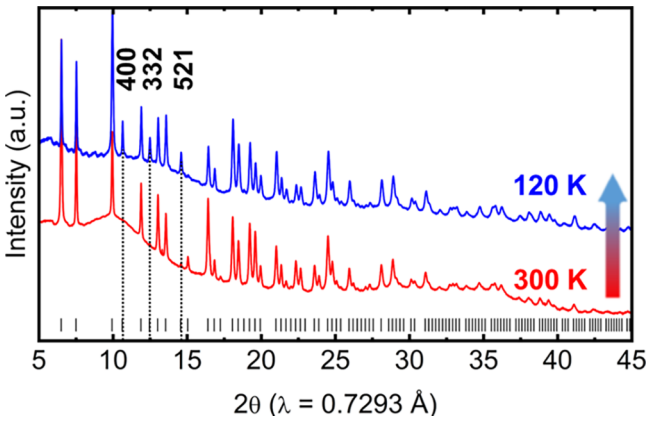

Figure 3. PXRD patterns for γ-$Mg(BH_4)_2$ at 300 K (red) and 120 K (blue). The locations of reflections associated with the γ-$Mg(BH_4)_2$ structure are shown as ticks below. The Miller indices are labeled for the three primary reflections enhanced in the low-temperature data. Intensities are logarithmically scaled to emphasize peaks across the full angular range.

intermediate complex during the synthesis of γ-$Mg(BH_4)_2$, we hypothesized that the increases in diffraction peak intensities of the 400, 332, and 521 reflections at low temperature are associated with localized "guest molecules" (presumably DMS, which can exhibit strong electron-donor interactions[25]) occupying the void space of γ-$Mg(BH_4)_2$ despite efforts to remove all coordinated solvents. Elemental analysis indicated that the γ-$Mg(BH_4)_2$ material contained 2.84 wt % sulfur and 2.39 wt % carbon, thus confirming the presence of impurity DMS. Excess carbon impurities can be accounted for by a small amount of *n*-heptane or toluene, the solvents of the dibutylmagnesium and borane DMS reactants in eq 2.

A Rietveld refinement (with results displayed in Figure S2) was performed on the low-temperature PXRD data from γ-$Mg(BH_4)_2$ in order to substantiate this hypothesis. Modeling of the γ-$Mg(BH_4)_2$ structure with DMS located at select sites within the pores was used to verify whether changes to the γ-phase diffraction pattern upon cooling were due to impurity molecules. To set up the structural model for a Rietveld refinement, the center of mass of DMS was initially placed at two distinct crystallographic sites: (0, 0, 0) and (1/8, 1/8, 1/8), each with 16-fold multiplicities, which can be visually observed in Figure S3a,b, respectively. Monte Carlo simulated annealing (MCSA) cycles were individually performed on the DMS molecules on both crystallographic sites in order to identify the optimal positions and orientations. The MCSA routine converged with the long axis of DMS oriented along the long axis of the cylindrical pores and remained fixed on the two 16b crystallographic sites. Since only the molecular centers of mass were positioned on the special sites, the DMS atoms resided on general sites (multiplicity = 96) which resulted in a sixfold orientational distribution of the DMS molecule about the long axis of the cylindrical pore. While allowing site occupations to vary, the final Rietveld refinement converged with an empirical formula of $Mg(BH_4)_2 \cdot 0.11\ S(CH_3)_2$ (R_{wp} = 2.845%) suggesting that an appreciable quantity of DMS impurities remains trapped within the material even after post-synthesis de-solvation. The refined stoichiometry amounts to ~5.8 wt% sulfur which is consistent with the elemental analysis, accounting for the slight variability in the quantity of DMS across γ-$Mg(BH_4)_2$ samples depending on storage duration/conditions [γ-$Mg(BH_4)_2$ samples outgas DMS upon storage]. It is noteworthy that DMS situated at (0,0,0) is centered in the hexagonal rings of BH_4 units, which optimizes the number of nearest neighbor interactions between DMS and BH_4. The refinement suggests that the (0,0,0) site (and equivalent crystallographic sites) is roughly 7 times more occupied by DMS than the (1/8,1/8,1/8) sites which reside at the center of the trigonal BH_4 units (i.e., the tangential points that give rise to the triply periodic porosity). The direct coordination of DMS with BH_4 units, observed here for γ-$Mg(BH_4)_2$, may explain the difficulty in removing impurity/solvent molecules from the γ-phase material and other $Mg(BH_4)_2$ phases [including ethers from α-$Mg(BH_4)_2$].[25]

Nitrogen physisorption measurements at 77 K were performed to complement the SAXS results and provide additional insights into the porosity of $Mg(BH_4)_2$. These measurements were performed on the as-synthesized γ-$Mg(BH_4)_2$ material without additional processing to remove solvent impurities other than the initial evacuation step necessary for physisorption. The raw nitrogen physisorption data is provided in Figure S4. Earlier work[12] suggested that γ-$Mg(BH_4)_2$ exhibits a theoretical specific surface area of 1500 m^2/g, though the same report's nitrogen physisorption data and BET analysis indicated a surface area of only 246 m^2/g. BET analysis performed on our nitrogen physisorption data indicates a surface area of 920 m^2/g (Figure S5), a value substantially higher than that reported previously. The corresponding PSD, displayed in Figure S6, from the N_2 physisorption measurements shows a distribution of pore

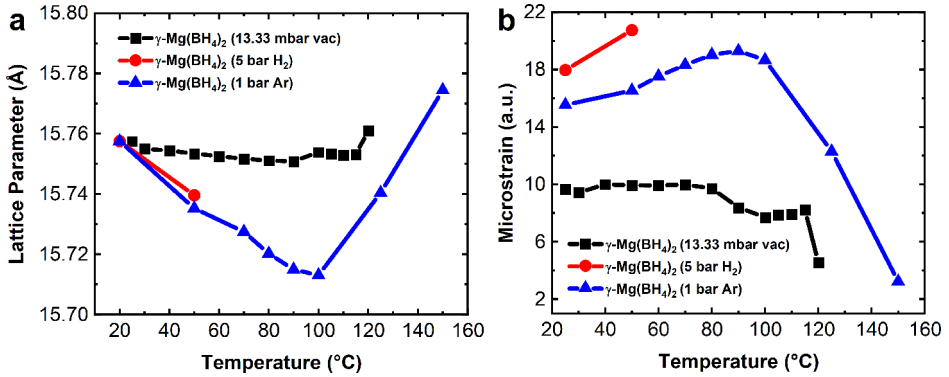

Figure 4. Temperature dependence of γ-$Mg(BH_4)_2$ lattice parameter (a) and microstrain-induced peak-broadening parameter (b) under a 13.33 mbar dynamic vacuum (black squares), 5 bar H_2 (red circles), and 1 bar argon (blue triangles) derived from sequential Rietveld refinements.

https://doi.org/10.1021/acs.chemmater.2c02925
Chem. Mater. 2022, 34, 10940−10951

width centered at 24 Å, a finding consistent with the length component of the pores determined from SAXS. We conjecture that the differences in cumulative surface areas and PSDs between prior work and the current study result from conditions used to isolate the final γ-$Mg(BH_4)_2$ structure. In both cases, the presence of residual solvent molecules explains both the low surface areas relative to the theoretical void space (as some pores are blocked) and the limited pore length obtained from SAXS measurements.

Crystal Structure of γ-$Mg(BH_4)_2$ as a Function of Temperature. With newfound knowledge of impurity molecules confined within the pores of γ-$Mg(BH_4)_2$, the materials were heated between room temperature and 300 °C under 1 bar argon (ambient pressure), 5 bar hydrogen, and dynamic vacuum (P_{base} = 13.33 mbar) in order to investigate the dependence of phase formation and associated transition temperatures on the in situ measurement environment. Due to the extensive nature of the data, the full sets of in situ PXRD patterns for all three environments are provided in the Supporting Information (see Figures S7, S8, and S9). Between room temperature and 100 °C, the γ-phase displays negative thermal expansion (NTE), observed in Figure 4a, which is commonly associated with the presence of guest molecules in porous frameworks.[44] For NTE to occur, attractive forces between the framework and confined guest molecules must be sufficient to induce a reduction of the framework volume. For γ-$Mg(BH_4)_2$, the NTE is affected by both the sample environment and perhaps, by extension, the presence of impurity guest molecules. The differences in magnitude of NTE in Figure 4a between γ-$Mg(BH_4)_2$ in ambient pressure argon and dynamic vacuum are notable. For example, at 100 °C, the lattice parameter of γ-$Mg(BH_4)_2$ differs by more than 0.04 Å between argon and vacuum environments which is greater than a factor of 10 in terms of lattice strain. XRD from γ-$Mg(BH_4)_2$ pressurized to 5 bar H_2 (see Figure S9) indicates that above 50 °C, the γ-phase transitions completely to the ε-phase, and as a result, data in Figure 4a,b are limited to ≤50 °C. An abrupt inflection of the lattice parameter (i.e., a transition from NTE to positive thermal expansion) is observed at 100 °C and represents the temperature at which residual DMS is desorbed from the framework, a presumption later confirmed by TPD. Results from sequential refinements of these PXRD data as a function of temperature between 20 and 120 °C also demonstrate an increase in microstrain-induced peak broadening[b] up to 100 °C (see Figure 4b). Coincidentally, there is an abrupt reduction in peak broadening between 100 and 120 °C as localized strains (measured by distributions of lattice parameters from their ideal values) in the γ-phase crystal lattice are reduced when DMS is expelled. The changes in microstrain-induced peak broadening arise concurrently with the turnover to positive thermal expansion. We suggest that both properties are related to the presence and subsequent expulsion of DMS impurities near 100 °C. When γ-$Mg(BH_4)_2$ is heated under dynamic vacuum, the impacts of microstrain and NTE are considerably dampened compared to those of the two other sample environments. These observations provided an indication that heating under dynamic vacuum facilitates the efficient removal of DMS impurities from the γ-phase framework and can be used as a post-processing technique for enhancing the purity of $Mg(BH_4)_2$ materials by removing undesired solvents and reducing their impact on the properties of the crystal structure such as microstrain. It remains unclear if the γ-$Mg(BH_4)_2$ structure can be completely de-solvated by heat treatment in vacuo or if substitution of sequentially weaker coordinating molecules is required to prevent collapse of the pore structure, as is the case for many metal organic frameworks.[45]

To further investigate the temperature-dependent structural response of $Mg(BH_4)_2$ and whether it is related to the release of impurities trapped in the porous network, TPD measurements were performed on γ-$Mg(BH_4)_2$. TPD from a sample of α-$Mg(BH_4)_2$, also prepared by the organomagnesium metathesis route (described in eq 2), was performed as a "control" measurement since the narrow pore α-phase structure should not desorb trapped solvent molecules at low temperatures. Due to the differing experimental conditions (e.g., evacuation rate, temperature gradients, heating rate), the temperatures at which events are observed in TPD are anticipated to be slightly higher than those of analogous events in PXRD.[c] The TPD data displayed in Figure 5 show that when the γ-phase sample

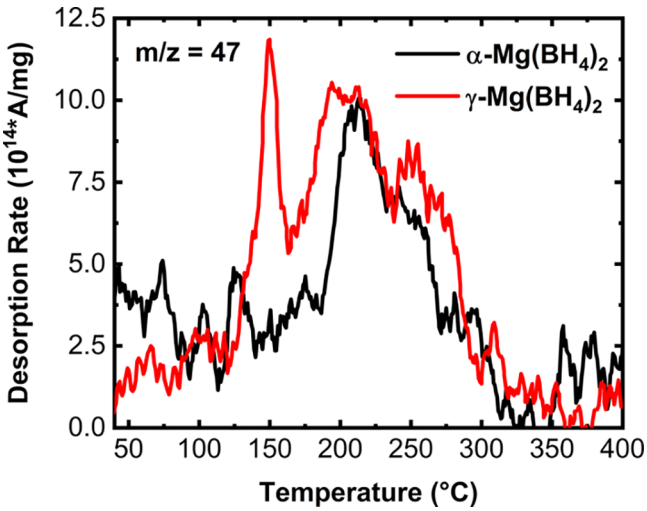

Figure 5. Mass-normalized TPD of m/z = 47 (representing DMS) from α- (black) and γ-phases (red) of $Mg(BH_4)_2$ between room temperature and 400 °C.

is heated, a spike in the signal representative of DMS, $S{\cdot}CH_3$, or its borane adduct $DMS{\cdot}BH_3$ at m/z = 47 is observed in the TPD starting at 125 °C and reaches maximum intensity near 150 °C. Above this temperature, a more gradual increase in the DMS signal occurs until a maximum is observed near 210 °C (i.e., the temperature of complete β-phase conversion) and subsides by 300 °C. When α-$Mg(BH_4)_2$ is heated, DMS is not released until approximately 200 °C and occurs as a broad peak in contrast to the sharp initial peak at lower temperatures observed for the γ-phase. We expect the α-phase to have nominally equivalent amounts of DMS impurities as the γ-phase since both polymorphs are synthesized by the same method. The higher-temperature initial release of DMS from the alpha phase may be due to the narrower corkscrew-shaped pore network of α-$Mg(BH_4)_2$ and the restricted desorption of solvent molecules. We find that the onset temperature (~125 °C) at which DMS is released from the γ-phase in the TPD measurements compares well with the inflection points of NTE and microstrain peak broadening determined previously from the in situ PXRD data.

Intermediate Epsilon Phase. It is important to preface the following discussion by noting that the temperature-resolved diffraction data were collected at or near thermody-

https://doi.org/10.1021/acs.chemmater.2c02925
Chem. Mater. 2022, 34, 10940−10951

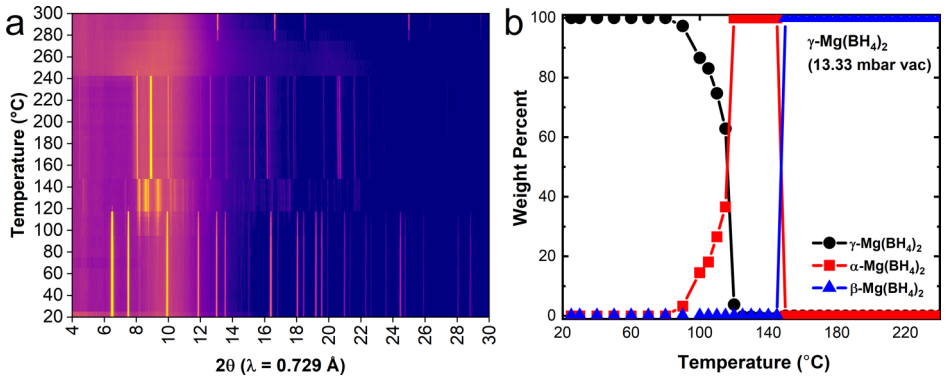

Figure 6. (a) In situ PXRD patterns near thermodynamic equilibrium for γ-$Mg(BH_4)_2$ heated between 20 and 220 °C under dynamic vacuum. (b) Weight fractions of crystalline $Mg(BH_4)_2$ phases as a function of sample temperature, derived from sequential Rietveld refinements of γ-$Mg(BH_4)_2$ in the dynamic vacuum environment. The XRD peaks present at ≥280 °C are due to the formation of MgH_2.

namic equilibrium (i.e., the temperature was not increased further until the diffraction pattern remained unchanged). The kinetics of these structural transformations are relatively slow, and prior reports[5,28] may have employed prohibitively short equilibration times. As γ-$Mg(BH_4)_2$ is heated to temperatures above 100 °C, a subset of diffraction peaks appear in PXRD which have been identified previously as the ε-phase.[5] Our data suggest that the temperature of formation and relative abundance of this phase are influenced by the sample environment. For example, the 5 bar hydrogen pressure induces formation of the ε-phase as low as 50 °C which may be an indication that the presence of ε-$Mg(BH_4)_2$ is related to pore collapse of the γ-phase. To date, the structure of the ε-phase has not been solved, and attempts at assigning symmetry to the unknown structure have been inconclusive.[5,28] The difficulty of determining the structure of the ε-phase is, in part, due to the inability to isolate ε-$Mg(BH_4)_2$ since it only forms by heating γ-$Mg(BH_4)_2$. Interestingly, if the heating is carried out slowly where measurements are acquired at discrete temperatures and thermodynamic equilibrium is nominally established at each step (e.g., 20 to 100 °C, over 1 h) under dynamic vacuum, formation of the ε-phase is suppressed, and a direct γ- to α-$Mg(BH_4)_2$ conversion is observed as shown in Figure 6a. Corresponding weight fractions of the known crystalline $Mg(BH_4)_2$ phases present during heating under dynamic vacuum were derived from sequential Rietveld refinements and are plotted as a function of temperature in Figure 6b. The weight fractions suggest that the γ- to α-phase transformation begins at as low as 90 °C. In a second in situ heating measurement under dynamic vacuum, the temperature of the γ-$Mg(BH_4)_2$ starting material was rapidly increased from 20 to 100 °C in 10 min which promoted higher relative intensities of peaks associated with the ε-phase (highlighted in Figure S10) with only a minor contribution from α-$Mg(BH_4)_2$. A visual comparison between both data sets is shown in Figure 7a,b with corresponding plots of the "fast" and "slow" heating programs displayed in Figure S11. It is also worth noting that the rapid heating and formation of ε-$Mg(BH_4)_2$ in high concentrations are always accompanied by the presence of the β-phase. This co-existence of ε- and β-phases is a feature shared among ε-$Mg(BH_4)_2$ formed in all three sample environments.

We believe that there are two plausible explanations for the observations discussed above. The first possibility (option **A**) requires that the γ-phase structure is the minimum energy state at room temperature (at least in the presence of adducted

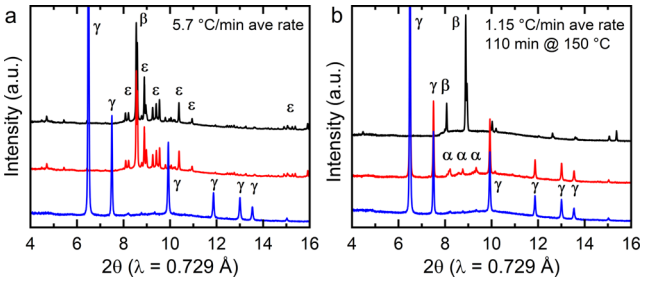

Figure 7. PXRD patterns from γ-$Mg(BH_4)_2$ heated (a) rapidly and (b) slowly at 25 (blue), 100 (red), and 160 °C (black) under dynamic vacuum.

DMS). At slightly elevated temperatures (~90 °C), the α-phase becomes the minimum energy structure. Because the structural transformation from γ- to α-$Mg(BH_4)_2$ is kinetically hindered, thermodynamic equilibrium is not established during rapid heating experiments. At higher temperatures (~150 °C), any remaining γ-$Mg(BH_4)_2$ converts directly to the stable β-phase structure causing the formation of a metastable transition state defined as the ε-phase of $Mg(BH_4)_2$. Alternatively, it is possible that the α-phase structure is the minimum energy structure below the β-$Mg(BH_4)_2$ transition temperature (option **B**). This necessitates that γ-$Mg(BH_4)_2$ is a metastable structure templated by the presence of a persistent coordinated solvent. The diffraction peaks assigned to the ε-phase are the result of either (**B1**) a short-lived species formed during the γ- to α-phase transition or (**B2**) a reaction between $Mg(BH_4)_2$ and DMS. The latter possibility, **B**, is supported by two key observations: (1) Any material shown to display diffraction peaks corresponding to ε-$Mg(BH_4)_2$ converts completely to the α-phase upon cooling to room temperature. (2) When left idle in an inert environment over long periods of time (~2 years), PXRD indicated that a complete γ- to α-$Mg(BH_4)_2$ conversion occurred. It is worthwhile to note that a similar scenario is observed when the $Mg(BH_4)_2{\cdot}0.50\ S(CH_3)_2$ intermediate structure is heated in ambient pressure argon. Richter et al.[14] observed that the $Mg(BH_4)_2{\cdot}0.5\ S(CH_3)_2$ complex forms pure α-$Mg(BH_4)_2$, followed by the phase denoted "ζ-$Mg(BH_4)_2$" near 225 °C. Based on the limited diffraction data available, it is not clear whether the ζ-phase is a product of residual DMS or related decomposition products. Regardless of the actual mechanism, our results suggest that ε-$Mg(BH_4)_2$ is a metastable intermediate formed only when the increase in temperature

https://doi.org/10.1021/acs.chemmater.2c02925
Chem. Mater. 2022, 34, 10940−10951

outpaces the slow transformation from γ- to α-$Mg(BH_4)_2$. Although Paskevicius et al.[28] previously reported that the ε-phase converts to α-$Mg(BH_4)_2$ upon cooling to room temperature, this is the first report providing evidence of the direct γ- to α-phase transformation during heating.

The prior literature[11] has indicated that when $Mg(BH_4)_2$ is heated to temperatures above ~185 °C, the ε- and/or α-phases irreversibly transform into the orthorhombic β-$Mg(BH_4)_2$ phase. Recalling the structural transformation from γ- to α-$Mg(BH_4)_2$ discussed in the previous section, the PXRD data acquired in this study near thermodynamic equilibrium (shown in Figure 6a) demonstrate that when the γ-phase is used as the starting material, the structural transformation from α- to β-$Mg(BH_4)_2$ proceeds at temperatures as low as 150 °C over a period of ~90 min. The complete set of PXRD data showing the slow kinetic conversion from α- to β-$Mg(BH_4)_2$ is provided in the Supporting Information (Figure S12).

The β-phase of $Mg(BH_4)_2$ has a remarkably large unit cell (V = 7439.82 Å^3), and its exact structure remains a subject of contention in the literature. Her et al.[11] first reported PXRD evidence of the β-phase and initially refined the crystal structure with *Immm* space group symmetry. They later determined that the *Immm* solution was representative of the spatially averaged structure and amended the structural model using an *Fddd* 2 × 2 × 2 supercell lattice. Doubling the lattice parameters of the *Immm* structure was necessary to account for the presence of broadened diffraction peaks unaccounted for by the original *Immm* structural description. In the *Fddd* model, the peaks left out of the initial refinement were able to be indexed as odd-hkl reflections severely broadened as a function of the increasing h-index. Although it was initially suggested that the broadening was a consequence of antiphase defects, Pitt et al.[46] appropriately noted that any number of microstructural defects which impact the coherence length can have the same effect on the powder averaged diffraction pattern. After the γ- to β-phase transformation pathway was published, a later report[5] denoted β-$Mg(BH_4)_2$ derived from the γ-phase β', "a more disordered form of the β-phase" which was a statement provided without clarification.

To investigate the claim of additional disorder in the so-called "β'-phase", X-ray scattering measurements were performed on the samples of β-$Mg(BH_4)_2$ generated from the γ-phase and compared to the results from the β-phase structure derived from the α-phase. In situ PXRD measurements were used to determine if the sample environment contributes to an additional degree of disorder in β-$Mg(BH_4)_2$. PXRD data for β-$Mg(BH_4)_2$ generated from the γ-phase material under dynamic vacuum, 1 bar argon, and 5 bar hydrogen all exhibit nominally the same diffraction patterns (i.e., peak locations, relative peak intensities, sample-induced peak broadening) at 200 °C, as shown in Figure 8. Additionally, the diffraction from β-$Mg(BH_4)_2$ annealed in the three sample environments cannot be differentiated from the published results of Her et al.[11] and Pitt et al.[46] Thus, we believe that the crystalline structures of β-$Mg(BH_4)_2$ are equivalent, regardless of the synthesis route.

However, our equilibrated PXRD data shown in Figure 6a suggest that the loss of diffraction from crystalline β-$Mg(BH_4)_2$ actually occurs near 240 °C, in contrast with a proposed amorphization and/or decomposition temperature of 280 °C reported previously.[5] Since the diffraction results indicated that the crystalline β-$Mg(BH_4)_2$ structures are equivalent, it was not clear whether the loss of diffraction from β-$Mg(BH_4)_2$ at lower

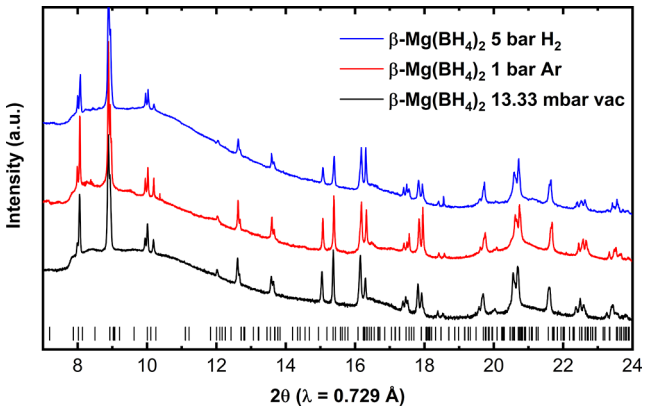

Figure 8. In situ PXRD of β-$Mg(BH_4)_2$ at 200 °C generated from the γ-$Mg(BH_4)_2$ starting material under dynamic vacuum (black), 1 bar argon (red), and 5 bar hydrogen (blue). Intensities are displayed with logarithmic scaling to emphasize the high angle data. Tick marks denote the locations of reflections from the published β-$Mg(BH_4)_2$ structure.[46]

temperatures was a consequence of the sample environment, thermal treatment, or other factors. Crystalline MgH_2 forms between 270 and 280 °C which firmly establishes a lower limit in temperature for hydrogen release explicitly due to $Mg(BH_4)_2$ decomposition.

In situ temperature-dependent SAXS–WAXS measurements, shown in Figure 9, were also performed on the γ-$Mg(BH_4)_2$ material to understand how the porosity and microstructure of the γ-phase evolve during the structural transformations previously discussed. When γ-$Mg(BH_4)_2$ is used as the starting material and heated under dynamic vacuum to generate the β-phase, a Guinier knee associated with the presence of pores remains observable in the SAXS data (see Figure 10a) similar to that observed previously for the γ-phase in Figure 2a. Simultaneous WAXS confirms that the material was successfully converted to the β-phase of $Mg(BH_4)_2$. The observation of porosity in the SAXS data was surprising provided the fact that the reported structure for β-$Mg(BH_4)_2$ exhibits no void space. An identical series of in situ temperature-resolved SAXS measurements were performed on a sample of α-$Mg(BH_4)_2$ (shown in Figure S13), also synthesized by the organomagnesium (eq 2) route. These data show that the progression from the α-phase to the β-$Mg(BH_4)_2$ structure is not accompanied by the same Guinier knee as that observed in Figure 9 which suggests that porosity in β-$Mg(BH_4)_2$ is a structural feature unique to the γ-phase pathway. With this information in mind, we concluded that the porosity observed for β-$Mg(BH_4)_2$ in SAXS must be "skeletal" (i.e. void space in between crystallites) and forms as a result of the transformation between the low-density γ-phase (0.55 g/cm^3)[12] and the higher-density α- (0.78 g/cm^3)[21] and β-phases (0.76 g/cm^3).[11] The ~38% increase in density between the γ- and β-phases is accompanied by an abrupt decrease in volume which would lead to intergranular void space. This type of volume reduction leading to porosity has also been observed in thermally decomposed ammoniate complexes[47,48] and dehydrided MgH_2.[49] BET analysis of N_2 physisorption data from a sample of γ-$Mg(BH_4)_2$, heated to 100 °C and subsequently cooled to room temperature [thus forming α-$Mg(BH_4)_2$ from the γ-phase], indicates that the specific surface area of the powder is 376 m^2/g. This value suggests that even though the material was converted to the α-phase (with no useable

https://doi.org/10.1021/acs.chemmater.2c02925
Chem. Mater. 2022, 34, 10940−10951

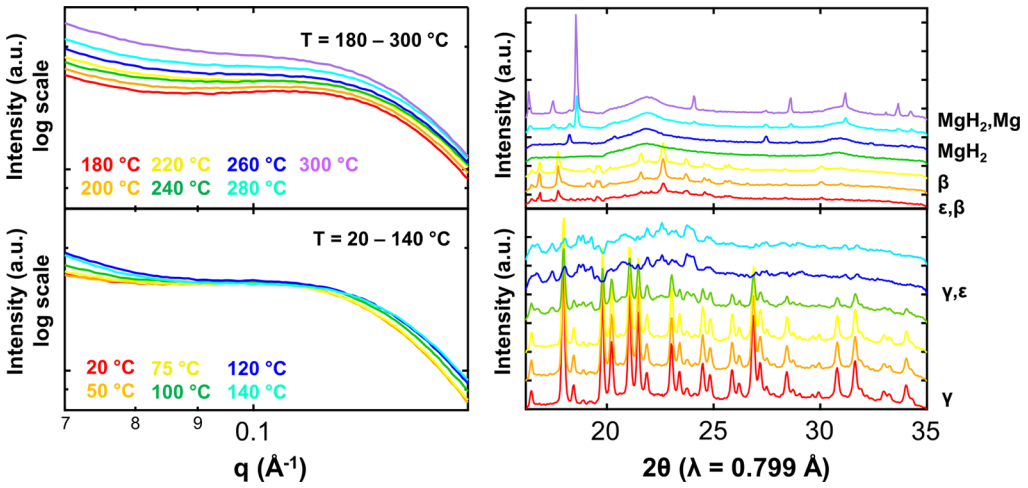

Figure 9. In situ temperature-resolved SAXS (left)−WAXS (right) data on γ-$Mg(BH_4)_2$ heated between 20 and 300 °C.

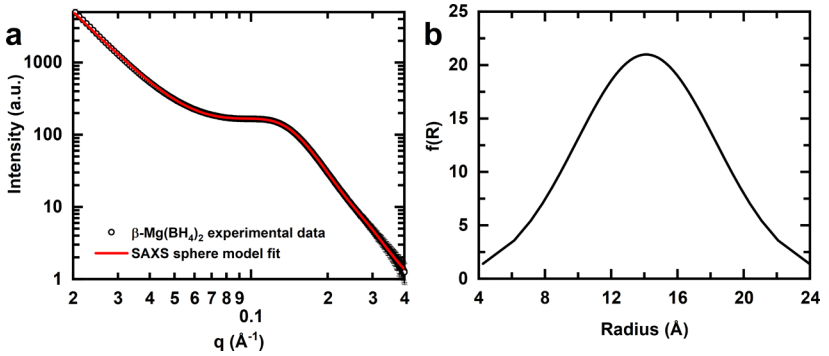

Figure 10. (a) Experimental SAXS data (black circles) from β-$Mg(BH_4)_2$ generated from the γ-phase at 220 °C and the corresponding size distribution fit (red line) to the experimental data using a spherical form factor. (b) Size distribution of spherical pore radii, $f(R)$, derived from the SAXS model.

crystalline porosity[12]), some amount of the skeletal porosity evolved is externally accessible to nitrogen molecules (see Figures S14 and S15).

Using the assumption that these skeletal pores are irregular in shape and randomly oriented, the SAXS model for data from β-$Mg(BH_4)_2$ (γ-phase heated to 200 °C) shown in Figure 10a suggests that the spherical pore radii (see Figure 10b) exhibit a Gaussian distribution of lengths centered around ∼14 Å. A structure factor contribution was also apparent with a correlation length of 41.05 Å and a packing factor of 2.11, both exhibiting decreases in magnitude from the γ-phase pore−pore correlation values (43.866 Å, 2.91 packing factor) presented earlier. It is possible that the locations of pores are partially templated by the original γ-$Mg(BH_4)_2$ porous framework structure which gives rise to inter-pore correlations in the skeletal network.

TEM images of γ-$Mg(BH_4)_2$ at room temperature (Figure 11a) and 250 °C (Figure 11b) acquired with identical location tracking confirmed the skeletal porosity (i.e., porosity within particles/grains but not necessarily within the crystal lattice) observed in the SAXS measurements. The TEM image from the $Mg(BH_4)_2$ particles heated to 250 °C exhibited decreases in the dark field signal relative to images from the material before heating. The particles were also visibly less dense with "pinholes" distributed throughout the material following heat treatment. Additionally, BET analysis from N_2 physisorption measurements (see Figure S16) indicates that the β-$Mg(BH_4)_2$

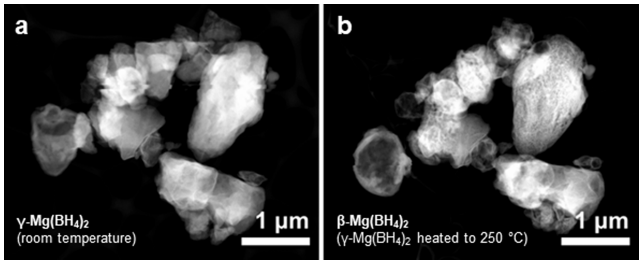

Figure 11. Identical location TEM images of γ-$Mg(BH_4)_2$ at (a) room temperature and (b) the same sample heated to 250 °C.

powder generated from the γ-phase starting material exhibits a specific surface area of merely 9.03 m^2/g with a rather featureless PSD (Figure S17), meaning that the skeletal porosity detected by SAXS is externally inaccessible to gas molecules.

Although it was confirmed that the same crystalline structure of β-$Mg(BH_4)_2$ is formed regardless of the sample condition, it is apparent that the microstructure of $Mg(BH_4)_2$ is significantly different depending on the synthesis pathway and starting phase. These differences in the microstructure may impact the observed decomposition temperatures as evident by the release of hydrogen observed in TPD data (performed with equivalent experimental conditions) shown in Figure 12. It is likely that the low-temperature hydrogen release (∼120 °C) from γ-$Mg(BH_4)_2$ can be explained by the presence of residual DMS

https://doi.org/10.1021/acs.chemmater.2c02925
Chem. Mater. 2022, 34, 10940−10951

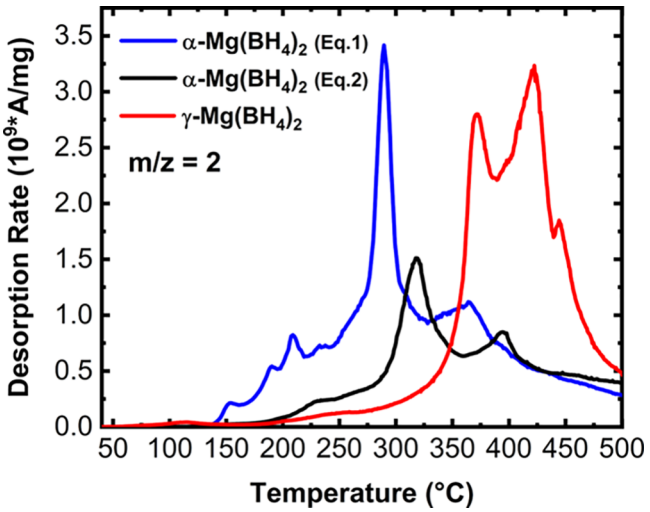

Figure 12. Mass-normalized TPD of hydrogen from all starting phases of $Mg(BH_4)_2$ between room temperature and 500 °C.

and thermally activated reactions with BH_4 units. However, the majority of hydrogen from the γ-$Mg(BH_4)_2$ starting material is not released until temperatures are higher than those of the α-$Mg(BH_4)_2$ analogues. It is currently unclear whether impurities (DMS or ethers) trapped within the narrow-pore α-phase structures cause lower temperatures of dehydrogenation. As seen from the in situ PXRD data on γ-$Mg(BH_4)_2$ presented in Figure 6, diffraction from β-$Mg(BH_4)_2$ disappears near 240 °C, and the possibility of polyborane formation at these temperatures will be the focus of a subsequent spectroscopic and ^{11}B nuclear magnetic resonance study.

CONCLUSIONS

Using synchrotron PXRD and SAXS, a comprehensive structural depiction of porous γ-$Mg(BH_4)_2$ and its temperature-dependent phase formation, outgassing, and decomposition was achieved. Results from PXRD at cryogenic temperatures demonstrate that the as-synthesized γ-phase of $Mg(BH_4)_2$ exhibits appreciable quantities of a coordinated solvent, even after post-synthetic drying. Heating the material under dynamic vacuum minimizes NTE experienced by the cubic γ-phase lattice, and solvent molecules are expelled from the pores above 100 °C which leads to a relaxation of the crystalline structure and direct conversion from γ- to α-$Mg(BH_4)_2$. Together, these results suggest that γ-$Mg(BH_4)_2$ is stabilized by the presence of a coordinated DMS solvent.

Rapid annealing of γ-$Mg(BH_4)_2$ causes the mutual formation of α- and ε-phases which indicates that the latter is potentially a short-lived transition phase encountered during the γ- to α-phase transformation or a disordered variant of α-$Mg(BH_4)_2$. PXRD results establish that the crystalline structures of β-$Mg(BH_4)_2$ are equivalent regardless of the starting material or sample environment. However, as $Mg(BH_4)_2$ evolves from the low-density γ-phase to the higher-density α- and/or β-phases, an abrupt decrease in cell volume is encountered which leads to skeletal porosity observed with SAXS and confirmed with TEM. Although the α- and γ-phase branches of the $Mg(BH_4)_2$ structural phase diagram converge upon formation of β-$Mg(BH_4)_2$, the differences in the microstructure (i.e., skeletal porosity) and impurity concentration (e.g., presence of coordinated DMS or ethers) give rise to diverging decomposition pathways as demonstrated by TPD. A follow-up study is underway in order to determine the effect of the identity and concentration of residual solvent molecules on the decomposition pathways of α- and γ-$Mg(BH_4)_2$ in an effort to determine the origin of different hydrogen release events in the TPD.

ASSOCIATED CONTENT

Supporting Information

The Supporting Information is available free of charge at https://pubs.acs.org/doi/10.1021/acs.chemmater.2c02925.

Porosity and helical arrangement of BH_4^- units in the γ-$Mg(BH_4)_2$ structure; Rietveld refinement of PXRD data for $Mg(BH_4)_2$ complexed to DMS; illustration of DMS locations in pores of γ-$Mg(BH_4)_2$; N_2 physisorption, BET analysis, and PSDs for as-synthesized and heated γ-$Mg(BH_4)_2$; in situ PXRD data for γ-$Mg(BH_4)_2$ heated in vacuum, argon, and H_2, between room temperature and 300 °C; PXRD data for ε-$Mg(BH_4)_2$; temperature program of heating under dynamic vacuum for PXRD measurements; PXRD data during slow conversion from α- to β-$Mg(BH_4)_2$ at 150 °C; and SAXS/WAXS data for thermal decomposition of α-$Mg(BH_4)_2$ (PDF)

AUTHOR INFORMATION

Corresponding Author

Thomas Gennett − *National Renewable Energy Laboratory, Golden, Colorado 80401, United States; Colorado School of Mines, Golden, Colorado 80401, United States;* Email: thomas.gennett@NREL.gov

Authors

Nicholas A. Strange − *National Renewable Energy Laboratory, Golden, Colorado 80401, United States; SLAC National Accelerator Laboratory, Menlo Park, California 94025, United States;* orcid.org/0000-0001-5699-7274

Noemi Leick − *National Renewable Energy Laboratory, Golden, Colorado 80401, United States;* orcid.org/0000-0002-2014-6264

Robert T. Bell − *National Renewable Energy Laboratory, Golden, Colorado 80401, United States;* orcid.org/0000-0003-0923-6012

Margaret A. Fitzgerald − *Colorado School of Mines, Golden, Colorado 80401, United States;* orcid.org/0000-0003-2976-0145

Svitlana Pylypenko − *Colorado School of Mines, Golden, Colorado 80401, United States;* orcid.org/0000-0001-7982-734X

Andreas Schneemann − *Sandia National Laboratories, Livermore, California 94550, United States;* orcid.org/0000-0001-6801-2735

Vitalie Stavila − *Sandia National Laboratories, Livermore, California 94550, United States;* orcid.org/0000-0003-0981-0432

Complete contact information is available at: https://pubs.acs.org/10.1021/acs.chemmater.2c02925

Notes

The authors declare no competing financial interest.

ACKNOWLEDGMENTS

This work was supported by the U.S. Department of Energy under contract no. DE-AC36-08GO28308 with the Alliance

for Sustainable Energy, LLC, the manager and operator of the National Renewable Energy Laboratory (NREL). Sandia National Laboratories is a multi-mission laboratory managed and operated by National Technology and Engineering Solutions of Sandia, LLC., a wholly owned subsidiary of Honeywell International, Inc., for the U.S. Department of Energy's National Nuclear Security Administration (NNSA) under contract DE-NA-0003525. The authors gratefully acknowledge research support from the Hydrogen Materials—Advanced Research Consortium (HyMARC), established as part of the Energy Materials Network under the U.S. Department of Energy, Office of Energy Efficiency and Renewable Energy, Fuel Cell Technologies Office, under contract no. DEAC36-08-GO28308. A.S. gratefully acknowledges the German Research Foundation (DFG) for a postdoctoral fellowship (SCHN 1539/1-1). XRD measurements were conducted at beamlines 2-1 and 7-2. SAXS measurement was performed at beamline 1-5. The authors acknowledge the support from skilled beamline scientists and engineers at SSRL including Kevin Stone, Chris Tassone, J.R. Troxel, Tim Dunn, and Bart Johnson. The authors also acknowledge useful discussions and technical input provided by Michael Toney. Use of the Stanford Synchrotron Radiation Lightsource, SLAC National Accelerator Laboratory, is supported by the U.S. Department of Energy, Office of Science, Office of Basic Energy Sciences, under contract no. DE-AC02-76SF00515. The views and opinions of the authors expressed herein do not necessarily state or reflect those of the United States Government or any agency thereof. Neither the United States Government nor any agency thereof, nor any of their employees, makes any warranty, expressed or implied, or assumes any legal liability or responsibility for the accuracy, completeness, or usefulness of any information, apparatus, product, or process disclosed or represents that its use would not infringe privately owned rights.

■ ADDITIONAL NOTES

[a]Within the united exponential/power law approximation for describing scattering from a rod, a structural level at low q is described by a Guinier exponential term related to the length dimension of the rod, followed by an intermediary power law decay with a Porod slope of −1 at increasing q. In this "two-level" structural model, at higher q values, a second Guinier structural level is observed and related to the cylindrical pore radius, followed again by a power law decay region with a Porod exponent of −4.

[b]Microstrain in this context is defined by a peak-broadening term, fwhm_{hkl} proportional to $\tan(\theta)$.

[c]TPD measurements were performed under dynamic high vacuum using a linear heating ramp and are explicitly non-equilibrium measurements as opposed to the in situ PXRD measurements which were performed at fixed temperatures and are considered to be in thermal equilibrium.

■ REFERENCES

(1) Newhouse, R. J.; Stavila, V.; Hwang, S. J.; Klebanoff, L. E.; Zhang, J. Z. Reversibility and Improved Hydrogen Release of Magnesium Borohydride. *J. Phys. Chem. C* **2010**, *114*, 5224−5232.

(2) White, J. L.; Strange, N. A.; Sugar, J. D.; Snider, J. L.; Schneemann, A.; Lipton, A. S.; Toney, M. F.; Allendorf, M. D.; Stavila, V. Melting of Magnesium Borohydride under High Hydrogen Pressure: Thermodynamic Stability and Effects of Nanoconfinement. *Chem. Mater.* **2020**, *32*, 5604−5615.

(3) Zavorotynska, O.; El-Kharbachi, A.; Deledda, S.; Hauback, B. C. Recent Progress in Magnesium Borohydride $Mg(BH_4)_2$: Fundamentals and Applications for Energy Storage. *Int. J. Hydrogen Energy* **2016**, *41*, 14387−14403.

(4) Heere, M.; Hansen, A.-L.; Payandeh, S.; Aslan, N.; Gizer, G.; Sørby, M. H.; Hauback, B. C.; Pistidda, C.; Dornheim, M.; Lohstroh, W. Dynamics of Porous and Amorphous Magnesium Borohydride to Understand Solid State Mg-Ion-Conductors. *Sci. Rep.* **2020**, *10*, 9080.

(5) David, W. I. F.; Callear, S. K.; Jones, M. O.; Aeberhard, P. C.; Culligan, S. D.; Pohl, A. H.; Johnson, S. R.; Ryan, K. R.; Parker, J. E.; Edwards, P. P.; Nuttall, C. J.; Amieiro-Fonseca, A. The Structure, Thermal Properties and Phase Transformations of the Cubic Polymorph of Magnesium Tetrahydroborate. *Phys. Chem. Chem. Phys.* **2012**, *14*, 11800−11807.

(6) Soloveichik, G. L.; Gao, Y.; Rijssenbeek, J.; Andrus, M.; Kniajanski, S.; Bowmanjr, R. C.; Hwang, S. J.; Zhao, J. C. Magnesium Borohydride as a Hydrogen Storage Material: Properties and Dehydrogenation Pathway of Unsolvated $Mg(BH_4)_2$. *Int. J. Hydrogen Energy* **2009**, *34*, 916−928.

(7) Yang, J.; Zhang, X.; Zheng, J.; Song, P.; Li, X. Decomposition Pathway of $Mg(BH_4)_2$ under Pressure: Metastable Phases and Thermodynamic Parameters. *Scr. Mater.* **2011**, *64*, 225−228.

(8) Li, H. W.; Miwa, K.; Ohba, N.; Fujita, T.; Sato, T.; Yan, Y.; Towata, S.; Chen, M. W.; Orimo, S. Formation of an Intermediate Compound with a $B_{12}H_{12}$ Cluster: Experimental and Theoretical Studies on Magnesium Borohydride $Mg(BH_4)_2$. *Nanotechnology* **2009**, *20*, 204013.

(9) Li, H. W.; Kikuchi, K.; Nakamori, Y.; Ohba, N.; Miwa, K.; Towata, S.; Orimo, S. Dehydriding and Rehydriding Processes of Well-Crystallized $Mg(BH_4)_2$ Accompanying with Formation of Intermediate Compounds. *Acta Mater.* **2008**, *56*, 1342−1347.

(10) Chong, M.; Karkamkar, A.; Autrey, T.; Orimo, S.; Jalisatgi, S.; Jensen, C. M. Reversible Dehydrogenation of Magnesium Borohydride to Magnesium Triborane in the Solid State under Moderate Conditions. *Chem. Commun.* **2011**, *47*, 1330−1332.

(11) Her, J. H.; Stephens, P. W.; Gao, Y.; Soloveichik, G. L.; Rijssenbeek, J.; Andrus, M.; Zhao, J. C. Structure of Unsolvated Magnesium Borohydride $Mg(BH_4)_2$. *Acta Crystallogr., Sect. B: Struct. Sci.* **2007**, *63*, 561−568.

(12) Filinchuk, Y.; Richter, B.; Jensen, T. R.; Dmitriev, V.; Chernyshov, D.; Hagemann, H. Porous and Dense Magnesium Borohydride Frameworks: Synthesis, Stability, and Reversible Absorption of Guest Species. *Angew. Chem.* **2011**, *123*, 11358−11362.

(13) Ban, V.; Soloninin, A. v.; Skripov, A. v.; Hadermann, J.; Abakumov, A.; Filinchuk, Y. Pressure-Collapsed Amorphous $Mg(BH_4)_2$: An Ultradense Complex Hydride Showing a Reversible Transition to the Porous Framework. *J. Phys. Chem. C* **2014**, *118*, 23402−23408.

(14) Richter, B.; Ravnsbæk, D. B.; Tumanov, N.; Filinchuk, Y.; Jensen, T. R. Manganese Borohydride; Synthesis and Characterization. *Dalton Trans.* **2015**, *44*, 3988−3996.

(15) Dai, B.; Sholl, D. S.; Johnson, J. K. First-Principles Study of Experimental and Hypothetical $Mg(BH_4)_2$ Crystal Structures. *J. Phys. Chem. C* **2008**, *112*, 4391−4395.

(16) Fan, J.; Bao, K.; Duan, D. F.; Wang, L. C.; Liu, B. B.; Cui, T. High Volumetric Hydrogen Density Phases of Magnesium Borohydride at High-Pressure: A First-Principles Study. *Chin. Phys. B* **2012**, *21*, 086104.

(17) Ozolins, V.; Majzoub, E. H.; Wolverton, C. First-Principles Prediction of a Ground State Crystal Structure of Magnesium Borohydride. *Phys. Rev. Lett.* **2008**, *100*, 1−4.

(18) Voss, J.; Hummelshøj, J. S.; Łodziana, Z.; Vegge, T. Structural Stability and Decomposition of $Mg(BH_4)_2$ Isomorphs - An Ab Initio Free Energy Study. *J. Phys.: Condens. Matter* **2009**, *21*, 012203.

(19) Zhou, X. F.; Oganov, A. R.; Qian, G. R.; Zhu, Q. First-Principles Determination of the Structure of Magnesium Borohydride. *Phys. Rev. Lett.* **2012**, *109*, 1−5.

https://doi.org/10.1021/acs.chemmater.2c02925
Chem. Mater. 2022, 34, 10940−10951

(20) Černý, R.; Filinchuk, Y.; Hagemann, H.; Yvon, K. Magnesium Borohydride: Synthesis and Crystal Structure. *Angew. Chem., Int. Ed.* **2007**, *46*, 5765−5767.
(21) Filinchuk, Y.; Černý, R.; Hagemann, H. Insight into $Mg(BH_4)_2$ with Synchrotron X-Ray Diffraction: Structure Revision, Crystal Chemistry, and Anomalous Thermal Expansion. *Chem. Mater.* **2009**, *21*, 925−933.
(22) Vitillo, J. G.; Bordiga, S.; Baricco, M. Spectroscopic and Structural Characterization of Thermal Decomposition of γ-$Mg(BH_4)_2$: Dynamic Vacuum versus H_2 Atmosphere. *J. Phys. Chem. C* **2015**, *119*, 25340−25351.
(23) Zavorotynska, O.; Deledda, S.; Li, G.; Matsuo, M.; Orimo, S. I.; Hauback, B. C. Isotopic Exchange in Porous and Dense Magnesium Borohydride. *Angew. Chem., Int. Ed.* **2015**, *54*, 10592−10595.
(24) Soloveichik, G.; Zhao, J.-C.Method for Manufacturing Magnesium Borohydride. U.S. Patent 20,070,140,944 A1, 2007.
(25) Zanella, P.; Crociani, L.; Masciocchi, N.; Giunchi, G. Facile High-Yield Synthesis of Pure, Crystalline $Mg(BH_4)_2$. *Inorg. Chem.* **2007**, *46*, 9039−9041.
(26) Richter, B.; Grinderslev, J. B.; Møller, K. T.; Paskevicius, M.; Jensen, T. R. From Metal Hydrides to Metal Borohydrides. *Inorg. Chem.* **2018**, *57*, 10768−10780.
(27) Jeong, S.; Heo, T. W.; Oktawiec, J.; Shi, R.; Kang, S.; White, J. L.; Schneemann, A.; Zaia, E. W.; Wan, L. F.; Ray, K. G.; Liu, Y.; Stavila, V.; Guo, J.; Long, R.; Wood, B. C.; Urban, J. A Mechanistic Analysis of Phase Evolution and Hydrogen Storage Behavior in Nanocrystalline $Mg(BH_4)_2$ within Reduced Graphene Oxide. *ACS Nano* **2020**, *14*, 1745−1756.
(28) Paskevicius, M.; Pitt, M. P.; Webb, C. J.; Sheppard, D. A.; Filsø, U.; Gray, E. M.; Buckley, C. E. In-Situ X-Ray Diffraction Study of γ-$Mg(BH_4)_2$ Decomposition. *J. Phys. Chem. C* **2012**, *116*, 15231−15240.
(29) Sahle, C. J.; Kujawski, S.; Remhof, A.; Yan, Y.; Stadie, N. P.; Al-Zein, A.; Tolan, M.; Huotari, S.; Krisch, M.; Sternemann, C. In Situ Characterization of the Decomposition Behavior of $Mg(BH_4)_2$ by X-Ray Raman Scattering Spectroscopy. *Phys. Chem. Chem. Phys.* **2016**, *18*, 5397−5403.
(30) Stadie, N. P.; Callini, E.; Richter, B.; Jensen, T. R.; Borgschulte, A.; Züttel, A. Supercritical N_2 Processing as a Route to the Clean Dehydrogenation of Porous $Mg(BH_4)_2$. *J. Am. Chem. Soc.* **2014**, *136*, 8181−8184.
(31) Sartori, S.; Knudsen, K. D.; Zhao-Karger, Z.; Bardaji, E. G.; Muller, J.; Fichtner, M.; Hauback, B. C. Nanoconfined Magnesium Borohydride for Hydrogen Storage Applications Investigated by SANS and SAXS. *J. Phys. Chem. C* **2010**, *114*, 18785−18789.
(32) Tsao, C. S.; Yu, M. S.; Wang, C. Y.; Liao, P. Y.; Chen, H. L.; Jeng, U. S.; Tzeng, Y. R.; Chung, T. Y.; Wu, H. C. Nanostructure and Hydrogen Spillover of Bridged Metal-Organic Frameworks. *J. Am. Chem. Soc.* **2009**, *131*, 1404−1406.
(33) Schneemann, A.; Wan, L. F.; Lipton, A. S.; Liu, Y. S.; Snider, J. L.; Baker, A. A.; Sugar, J. D.; Spataru, C. D.; Guo, J.; Autrey, T. S.; Jørgensen, M.; Jensen, T. R.; Wood, B. C.; Allendorf, M. D.; Stavila, V. Nanoconfinement of Molecular Magnesium Borohydride Captured in a Bipyridine-Functionalized Metal-Organic Framework. *ACS Nano* **2020**, *14*, 10294−10304.
(34) Hurst, K. E.; Heben, M. J.; Blackburn, J. L.; Gennett, T.; Dillon, A. C.; Parilla, P. A. A Dynamic Calibration Technique for Temperature Programmed Desorption Spectroscopy. *Rev. Sci. Instrum.* **2013**, *84*, 025103.
(35) Walton, K. S.; Snurr, R. Q. Applicability of the BET Method for Determining Surface Areas of Microporous Metal-Organic Frameworks. *J. Am. Chem. Soc.* **2007**, *129*, 8552−8556.
(36) Leick, N.; Strange, N. A.; Schneemann, A.; Stavila, V.; Gross, K.; Washton, N.; Settle, A.; Martinez, M. B.; Gennett, T.; Christensen, S. T. Al_2O_3 Atomic Layer Deposition on Nanostructured γ-$Mg(BH_4)_2$ for H_2 Storage. *ACS Appl. Energy Mater.* **2021**, *4*, 1150−1162.
(37) Ilavsky, J. Nika: Software for Two-Dimensional Data Reduction. *J. Appl. Crystallogr.* **2012**, *45*, 324−328.
(38) Ilavsky, J.; Jemian, P. R. Irena: tool suite for modeling and analysis of small-angle scattering. *J. Appl. Crystallogr.* **2009**, *42*, 347−353.
(39) Hoffman, A. S.; Singh, J. A.; Bent, S. F.; Bare, S. R. In Situ Observation of Phase Changes of a Silica-Supported Cobalt Catalyst for the Fischer-Tropsch Process by the Development of a Synchrotron-Compatible in Situ/Operando Powder X-Ray Diffraction Cell. *J. Synchrotron Radiat.* **2018**, *25*, 1673−1682.
(40) Toby, B. H.; Von Dreele, R. B. GSAS-II: The Genesis of a Modern Open-Source All Purpose Crystallography Software Package. *J. Appl. Crystallogr.* **2013**, *46*, 544−549.
(41) Speck, A. L.*PLATON*; Utrecht University: Utrecht, The Netherlands.
(42) Hanson, R. M. Jmol-a Paradigm Shift in Crystallographic Visualization. *J. Appl. Crystallogr.* **2010**, *43*, 1250−1260.
(43) Beaucage, G. Approximations Leading to a Unified Exponential/Power-Law Approach to Small-Angle Scattering. *J. Appl. Crystallogr.* **1995**, *28*, 717−728.
(44) Joo, J.; Kim, H.; Han, S. H. Volume Shrinkage of a Metal−Organic Framework Host Induced by the Dispersive Attraction of Guest Gas Molecules. *Phys. Chem. Chem. Phys.* **2013**, *15*, 18822−18826.
(45) Erhart, O.; Georgiev, P. A.; Krautscheid, H. Desolvation Process in the Flexible Metal−Organic Framework [Cu(Me-4py-Trz-Ia)], Adsorption of Dihydrogen and Related Structure Responses. *CrystEngComm* **2019**, *21*, 6523−6535.
(46) Pitt, M. P.; Webb, C. J.; Paskevicius, M.; Sheptyakov, D.; Buckley, C. E.; Gray, E. M. A. In Situ Neutron Diffraction Study of the Deuteration of Isotopic $Mg^{11}B_2$. *J. Phys. Chem. C* **2011**, *115*, 22669−22679.
(47) Jacobsen, H. S.; Hansen, H. A.; Andreasen, J. W.; Shi, Q.; Andreasen, A.; Feidenhans'l, R.; Nielsen, M. M.; Ståhl, K.; Vegge, T. Nanoscale Structural Characterization of $Mg(NH_3)_6Cl_2$ during NH_3 Desorption: An in Situ Small Angle X-Ray Scattering Study. *Chem. Phys. Lett.* **2007**, *441*, 255−260.
(48) Hummelshøj, J. S.; Sørensen, R. Z.; Kustova, M. Y.; Johannessen, T.; Nørskov, J. K.; Christensen, C. H. Generation of Nanopores during Desorption of NH3 from $Mg(NH_3)_6Cl_2$. *J. Am. Chem. Soc.* **2006**, *128*, 16−17.
(49) Dura, J. A.; Kelly, S. T.; Kienzle, P. A.; Her, J.-H.; Udovic, T. J.; Majkrzak, C. F.; Chung, C.-J.; Clemens, B. M. Porous Mg Formation upon Dehydrogenation of MgH_2 Thin Films. *J. Appl. Phys.* **2011**, *109*, 093501.

https://doi.org/10.1021/acs.chemmater.2c02925
Chem. Mater. 2022, 34, 10940−10951